ARTICLE OPEN ACCESS

Type II Hot Corrosion of Two Mo-Si-Ti Alloys and Mo-Si-B With a Salt Deposit of Mixed Na_2SO_4 and $NiSO_4$

Lukas Korell[1] | Katharina Beck[1] | Arun R. Chitra[2] | Frauke Hinrichs[3] | Ceyhun Oskay[1] | Emma White[1] | Martin Heilmaier[3] | Mathias C. Galetz[1]

[1]High Temperature Materials, DECHEMA Research Institute, Frankfurt am Main, Germany | [2]Institute for Applied Materials - Applied Material Physics, Karlsruhe Institute of Technology, Eggenstein-Leopoldshafen, Germany | [3]Institute for Applied Materials - Materials Science and Engineering, Karlsruhe Institute of Technology, Karlsruhe, Germany

Correspondence: Mathias C. Galetz (mathias.galetz@dechema.de)

Received: 13 June 2025 | **Revised:** 28 August 2025 | **Accepted:** 9 September 2025

Funding: Deutsche Forschungsgemeinschaft (DFG): 413956820.

Keywords: eutectic phases | hot corrosion | Mo-based alloys | molten salts | molybdates | Mo-Si-B | Mo-Si-Ti | Na_2SO_4 | $NiSO_4$ | pesting | silicides

ABSTRACT

To enhance turbine efficiencies by increasing gas inlet temperatures, new materials must be developed which can withstand harsh corrosive environments and provide sufficient mechanical properties at elevated temperatures. The hot corrosion behavior of the promising alloy candidates Mo-20Si-52.8Ti (at.%), Mo-21Si-34Ti (at.%) and Mo-9Si-8B (at.%) under mixed 60mol.% Na_2SO_4 and 40mol.% $NiSO_4$ deposit in dry synthetic air plus 0.1vol.% SO_2 were investigated at 700°C. Optical and electron microscopy, EPMA and XRD were employed for analysis. Comparing the results to tests with pure Na_2SO_4 reveals that the Mo content significantly impacts the corrosion attack if Ni is present. Na_2MoO_4 is observed during corrosion besides the initial eutectic phase between Na_2SO_4 and $NiSO_4$. With melting points below 700°C, both compounds are capable of dissolving the surrounding material. However, the formation of $NiMoO_4$ is energetically favored, transforming the initial liquid eutectic sulfate mixtures. Therefore the corrosion rate is lowered by the addition of $NiSO_4$ to the Na_2SO_4 deposit.

1 | Introduction

Refractory alloys are promising candidates for high temperature applications. Their high melting points can increase the maximum operating temperatures compared to Ni-based alloys, the state of the art in applications such as turbine blades [1, 2] and can operate at peak temperatures around 1150°C. Because of the high mechanical stability at elevated temperatures of refractory metals, they could be used to build combustion engines operating with metal temperatures up to 1600°C [1]. Increasing temperature and lower cooling losses leads to higher turbine efficiency [2, 3]. Thus there is a rising interest in developing new refractory alloys for ultrahigh temperature applications [4–6].

For any turbine material, along with a high mechanical strength, a high resistance against oxidation and corrosion is also necessary. One particular corrosive environment in the turbine is caused by molten salts that can be deposited on the surface behind the combustion chamber [7–10]. The formation of sodium sulfate from NaCl and SO_3 from sea salt and sulfur-based impurities in the fuel or air, respectively, is displayed in Equation 1 [8, 11]. Na_2SO_4 is the most important component in what became known as "hot corrosion" [8, 12–14].

$$2NaCl(g) + SO_3(g) + \frac{1}{2}O_2(g) \rightleftharpoons Na_2SO_4(l) + Cl_2(g) \quad (1)$$

In hot corrosion, two separate mechanisms are often distinguished. Type I hot corrosion is related to the melting of Na_2SO_4 at 884°C [15]. If this temperature is exceeded, the resulting liquid phase causes a uniform corrosion attack with a high corrosion rate [12, 16].

Low melting mixtures between the salt and corrosion products at lower temperatures can also induce hot corrosion, so called Type II. Common examples are the eutectic mixtures Na_2SO_4–$CoSO_4$ (T_m = 540°C) or Na_2SO_4–$NiSO_4$ (T_m = 670°C) [7, 8, 17, 18]. Type II hot corrosion is characterized by an incubation and a propagation stage, in which the formation of pits is generally observed [7, 19]. For the widely investigated Ni-based alloys, Type II attack usually occurs in the temperature range from 600°C to 750°C [20].

Even though Mo alloys have been investigated extensively due to their superior high temperature creep properties, they have an inherently low oxidation resistance in the same temperature range as hot corrosion because they suffer from catastrophic oxidation behavior by "pesting". Pesting is characterized by the dominant formation of volatile MoO_3 at the surface and the grain boundaries [21, 22], which leads to the complete disintegration of the material. Mo-Si-B alloys exhibit pesting between 650°C and 750°C, even though they can form a protective SiO_2 scale at higher temperatures up to 1300°C [23]. Recent work on alloys in the Mo-Si-Ti system, shows highly improved oxidation resistance in the critical temperature regime for MoO_3 evaporation [21, 24]. In oxidation experiments of the alloys Mo-21Si-34Ti (at.%) and Mo-20Si-52.8Ti (at.%) at 700°C and 900°C, a protective duplex scale of TiO_2 and SiO_2 formed on the surface [5, 21, 25, 26]. Therefore the resistance of Mo-based alloys against the more aggressive hot corrosion attack is of high interest.

If Mo is used as an alloying element in Ni-based alloys, it enhances the corrosion rate in the presence of Na_2SO_4 deposits [13]. When Na_2SO_4 is converted to Na_2MoO_4 with a melting point of 687°C, it can introduce fluxing and rapid corrosion [13, 27], as described in detail in [16, 28]. A recent study showed that the hot corrosion behavior of Mo-9Si-8B (at.%), Mo-20Si-52.8Ti (at.%) and Mo-21Si-34Ti (at.%) differs significantly from that of Ni-based alloys [28, 29]. Exposure of Mo-9Si-8B (at.%) in a SO_2 containing atmosphere with a Na_2SO_4 deposit at 700°C and 900°C resulted in a discontinuous SiO_2 layer that could not protect against pesting [29]. The Mo-21Si-34Ti (at.%) alloy underwent a mixture of pesting, dissolution and selective oxidation, while Mo-20Si-52.8Ti (at.%) was also dominated by pesting at 700°C, but formed a protective SiO_2 layer at 900°C.

In any future turbine designs, the material will most likely be used together with Ni-based alloys in other sections of gas turbine engines, and it is reasonable to assume that corrosion products such as $NiSO_4$ will be transferred to the surface of the Mo-based component. Along with the always omnipresent Na_2SO_4, the molten eutectic mixture of, Na_2SO_4–$NiSO_4$, well-known from Type II hot corrosion of Ni-based alloys [7, 19], will form. This eutectic can be found at a composition of 62mol.% Na_2SO_4 and 38mol.% $NiSO_4$ and has a melting point of approximately 670°C [30–33].

In this work three Mo-based alloys were coated with a mixture of the salts close to the eutectic composition (62mol.% Na_2SO_4, 38mol.% $NiSO_4$) and exposed to dry synthetic air + 0.1vol.% SO_2 at 700°C, above the melting point of the eutectic phase. The corroded samples were analyzed with XRD, SEM and EPMA, and the results were compared to experiments with pure Na_2SO_4 deposits at 700°C. The influence of the Mo content on the corrosion behavior of the Mo-based alloys in contact with the Ni-rich salt was investigated.

2 | Materials and Methods

2.1 | Investigated Alloys

To prepare the Mo-9Si-8B (at.%) alloy the elemental powders Mo (99.95%, HC Starck), Si (99.99%, Alfa Aesar), and B (98%, MaTeck) were mechanically alloyed using a planetary ball mill (Retsch PM 400) with WC balls, a powder-to-ball ratio of 1:12, and a speed of 200 rpm Cylindrical samples were produced using the field assisted sintering technique (FAST) at 1600°C and 50 MPa for 15 min. The resulting samples, which had a residual porosity of less than 2% [34], were subjected to a homogenization treatment at 1600°C for 100 h in Ar (99.998%).

The two Mo-Si-Ti alloys, eutectic Mo-20Si-52.8Ti (at.%) and eutectoid Mo-21Si-34Ti (at.%), were manufactured in an arc melter (Edmund Bühler GmbH AM/0.5). The used elemental materials are listed in Table 1.

After the chamber was evacuated and flooded with Ar (99.998%) three times, it was evacuated to 10^{-4} mbar. A Zr oxygen getter was remelted to further reduce the oxygen inside the chamber before melting of the alloys. The arc melting was done in a water-cooled copper crucible in a vacuum chamber with an Ar base pressure of 600 mbar. The ingots were remelted five times and flipped between each step to obtain homogeneous alloys. Mo-21Si-34Ti (at.%) was heat treated at 1300°C for 200 h under Ar atmosphere in a Gero HTRH 70-600/18 resistance tube furnace to achieve eutectoid decomposition [5].

Wire arc cutting was used to extract specimens out of each ingot. Specimens of 12 to 14 mm in diameter and 10 mm in height were cut from the Mo-Si-Ti rods. The cubic specimens produced from the Mo-Si-B had dimensions of 10 mm × 10 mm × 3 mm. After the cutting process, the samples were ground with P500 silicon carbide paper to remove Cu contamination, which could be introduced by wire erosion. Finally, all samples were cleaned with an ultrasonic bath in acetone.

2.2 | Hot Corrosion

For the hot corrosion experiments 2.5 mg/cm^2 of a mixture of 60% Na_2SO_4 and 40% $NiSO_4$ was deposited by evaporating a solution on the preheated samples. The samples were put in individual Al_2O_3 crucibles and placed in a quartz tube furnace (Carbolite VST 12/900). After a drying step at 150°C under

TABLE 1 | Elements used for arc-melting Mo-Si-Ti alloys with purity and supplier.

Element	Purity	Supplier
Mo	99.95%	EVOCHEM
Si	99.95%	ChemPUR
Ti	≥ 99.8%	ChemPUR

synthetic air for 12 h, the samples were exposed to dry synthetic air (99.99%, Air Liquide) mixed with 0.1vol.% SO_2 (99,98%, Air Liquide) with a flow rate of about 5 L/h and heated up to 700°C with a heating rate of 10°C/min. Experiments lasting 24 and 100 h were carried out to investigate the progression of hot corrosion over time. A Fe_2O_3 catalyst was placed at the gas inlet of the furnace to enable the oxidation of SO_2 in the gas mixture to SO_3:

$$SO_2 + \frac{1}{2}O_2 \rightleftharpoons SO_3 \quad (2)$$

After the experiment, the samples were cooled down to room temperature using natural cooling under pure synthetic air.

2.3 | Analytical Characterization

A Leica MZ16 stereomicroscope was used to take macroscopic images in the as-cast state and after the hot corrosion experiments. X-ray diffraction (XRD) measurements, were performed using a Bruker D8 Advance A25 and Cu-K_α radiation. Cross-sections of each sample were produced by cutting the samples in half and mounting them in an epoxy resin. The cross-sections were prepared using water-free metallographic methods including grinding to P 2400 using a series of silicon carbide papers. Diamond suspensions were used for polishing with 3 μm and 1 μm. After sputtering with graphite, a scanning electron microscope (SEM, Hitachi FlexSEM 1000II with an energy dispersive X-ray spectrometer (EDS)) was utilized to investigate the cross-sections. At least four separate measurements were averaged to determine the layer thicknesses and standard deviations. The formed phases are analyzed by combining the elemental distribution from the EPMA maps with the results from XRD and Raman spectroscopy. A JEOL JXA-8100 electron probe microanalyzer (EPMA), equipped with a wavelength-dispersive X-ray spectroscopy detector (WDS), was used to acquire concentration profiles and elemental maps. Raman spectroscopy (Renishaw inVia Raman Microscope) was conducted with a laser wavelength of 633 nm to analyze the formed oxides. Thermodynamic calculations were carried out using FactSage 8.2 software.

3 | Results

3.1 | Hot Corrosion of the Mo-9Si-8B (at.%) Alloy

Figure 1 shows the cross-section of the Mo-9Si-8B (at.%) alloy after exposure in a mixture of Na_2SO_4 and $NiSO_4$. The elemental distribution maps are displayed in Figure 1c and d.

Figure 1 shows the cross-section of the Mo-9Si-8B (at.%) alloy after exposure in a mixture of Na_2SO_4 and $NiSO_4$. The elemental distribution maps are displayed in Figure 1c,d. In Figure 1a,b it can be seen, that a SiO_2 scale formed, which protected the alloy from catastrophic corrosion. On the surface, solid oxides of $NiMoO_4$, MoO_3 and SiO_2 formed, with large cavities inside the scale.

Particles of MoO_3 and smaller amounts of Na_2MoO_4 inside the SiO_2 layer were identified based on EPMA. After 24 h, $NiMoO_4$ (identified by XRD and EPMA) accumulated on top of the SiO_2 layer, while Na_2MoO_4 was also found inside this layer and in the SiO_2 layer. After 100 h of hot corrosion $NiMoO_4$ was still seen on top of the oxide scale but not across the entire sample surface as after 24 h (see Figure 1). This suggests local spallation after 100 h, most likely during cooling, because MoO_3 was identified at the surface in Figure 1b, which would otherwise have evaporated if it had been lying openly on the surface at this temperature. For both exposure times, an oxide layer of mainly MoO_3 was observed in the electron microscopy images (Figure 1a,b) beneath the outer SiO_2 layer, as it was protected.

3.2 | Hot Corrosion of the Mo-21Si-34Ti (at.%) Alloy

The corroded Mo-21Si-34Ti (at.%) alloy samples after 24 and 100 h of hot corrosion at 700°C are presented in Figure 2.

The oxide layer which can be seen on both of the samples, mainly consists of a duplex scale with an outer layer of mixed SiO_2 and TiO_2, and an inner layer of $SiO_2/TiO_2/MoO_3$ (see Figure 2c,d, A1). After 24 h of hot corrosion $NiMoO_4$ was found on top of this layer as confirmed by XRD measurements (see A1). The needle shaped crystallites, which could be identified to be MoO_3 by Raman spectroscopy (see Figure A2), are visible inside the SiO_2/TiO_2 duplex scale.

After 100 h, no $NiMoO_4$ was found on the sample surface, but more MoO_3 needles were incorporated in the SiO_2 and TiO_2 scale (see Figure 1b). This scale was four times as large as after 24 h of hot corrosion. In contrast, the internal layer underneath was around 20 μm smaller after 100 h than after 24 h, while the overall oxide scale is thicker than for the Mo-Si-B alloy shown in Figure 1. When comparing the light microscopy images the metal wastage is the highest for Mo-21Si-34Ti (at.%), especially after 100 h. Again, the presence of MoO_3 is attributed to the mixed oxide scale, which decreased the evaporation rate of MoO_3.

3.3 | Hot Corrosion of the Mo-20Si-52.8Ti (at.%) Alloy

Figure 3 shows the cross-section of Mo-20Si-52.8Ti (at.%) after the hot corrosion test in Na_2SO_4 and $NiSO_4$. As for the Ti-lean eutectoid Mo-21Si-34Ti (at.%) alloy, hot corrosion attack led to the formation of a mixed oxide layer of SiO_2 and TiO_2 (see Figures 3 and A1). $NiMoO_4$ can be identified on the outer surface, as shown by XRD (see Fig A1). After 100 h there is less $NiMoO_4$ present than after 24 h. Despite the presence of the same oxides as Mo-21Si-34Ti (at.%) (see Figure 2), the scale is significantly (one order of magnitude) thinner for the eutectic alloy Mo-20Si-52.8Ti (at.%). By comparing the light microscopy images of the two Mo-Si-Ti alloys, the consumption of the sample is lower for the eutectic, Ti-rich alloy (comparing Figures 2f and 3f). The key difference is the scale thickness is around 25 µm after 24 h and stays around 25 µm after 100 h without showing a significant change in morphology for Mo-20Si-52.8Ti (at.%). Even though the top layer does appear fully dense (and protective), it evidently slows down the

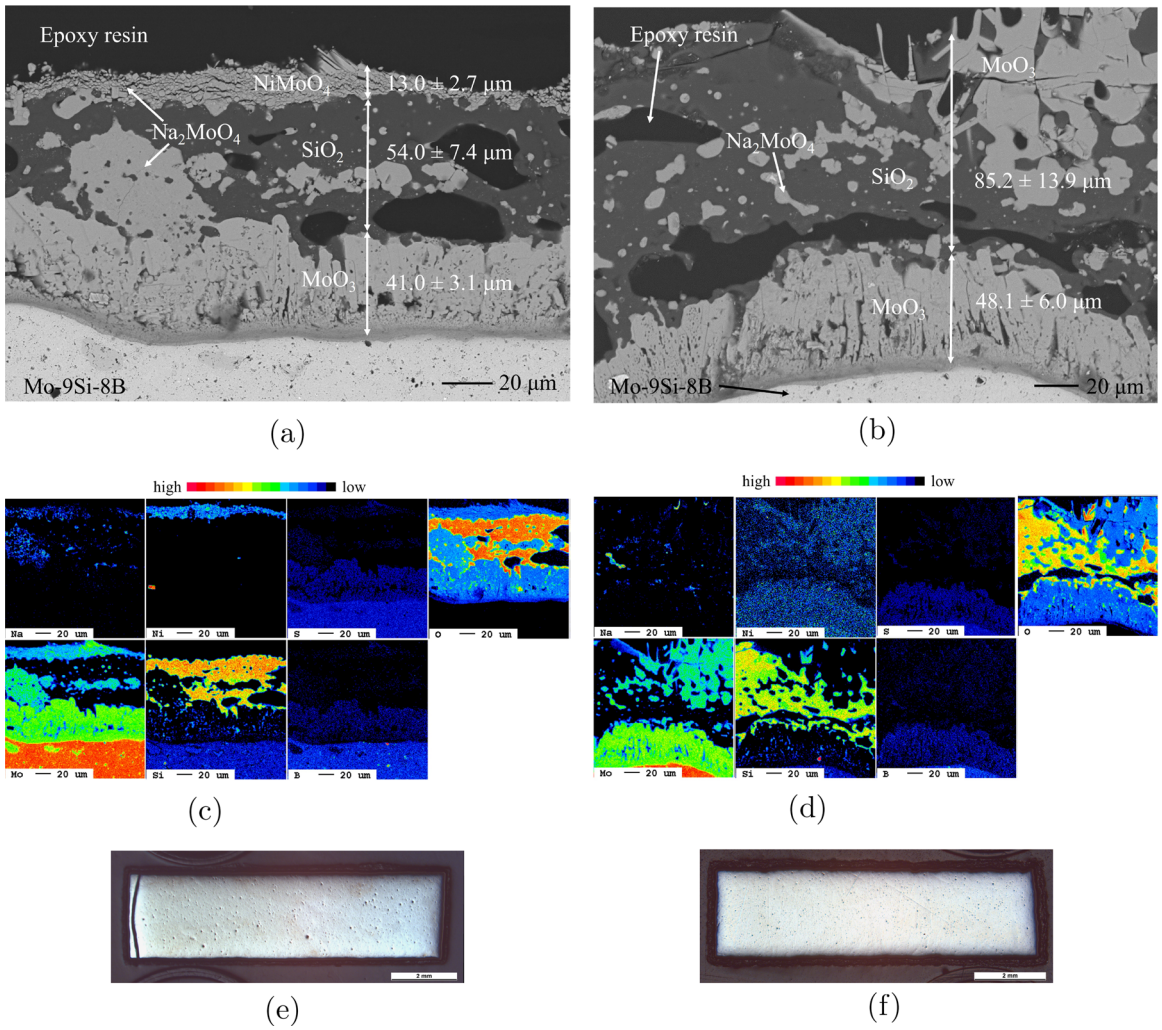

FIGURE 1 | BSE (a,c), EPMA (b,d) and optical microscopy (e,f) images of cross-sections after hot corrosion at 700°C in dry synthetic air + 0.1vol.% SO_2 with $NiSO_4/Na_2SO_4$ deposit. (a) Mo-9Si-8B (at.%) after 24 h, (b) Mo-9Si-8B (at.%) after 100 h, (c) Mo-9Si-8B (at.%) after 24 h, (d) Mo-9i-8B after 100 h, (e) Mo-9Si-8B (at.%) after 24 h, (f) Mo-9Si-8B (at.%) after 100 h. [Color figure can be viewed at wileyonlinelibrary.com]

corrosion process, as the increase of the oxide layer in thickness after 100 h is marginal.

4 | Discussion

The three-phase Mo–9Si–8B alloy is made up of a A2-type bcc solid solution phase (Mo_{SS}), a T2-type Mo_5SiB_2 phase and a A15-type Mo_3Si intermetallic compound. The lamellar microstructure of the two Mo-Si-Ti alloys consists of two phases, which are a Mo solid solution phase and a silicide phase. The silicide phase present in Mo-21Si-34Ti (at.%) is tetragonal ($(Mo,Ti)_5Si_3$), while in Mo-20Si-52.8Ti (at.%) it is hexagonal ($(Ti,Mo)_5Si_3$) [5]. The Mo_{SS} is prone to oxidation due to the higher Mo and lower Si content than the other phases.

For temperatures above 1000°C, Mo-Si-B alloys have a high resistance against hot corrosion due to the formation of a dense and protective SiO_2 scale, but they undergo pesting at lower temperatures resulting in catastrophic failure [14, 22, 35, 36]. The hot corrosion of the Mo-Si-B alloy is dominated by the competing effects of pesting and SiO_2 formation, as shown in [29]. The Mo-rich Mo-21Si-34Ti (at.%) showed a mixture of pesting, dissolution and selective oxidation during hot corrosion experiments [28]. With a lower Mo-content, Mo-20Si-52.8Ti (at.%) produced a protective SiO_2 layer at 900°C but was also dominated by pesting at 700°C [28].

Schematic illustration of the dominating corrosion mechanisms for the alloys are displayed in Figure 4. At the very initial stages of exposure, MoO_3 does not seem to evaporate but reacts with available $NiSO_4$ to form $NiMoO_4$ (Equation 3) and with Na_2SO_4 to form Na_2MoO_4 (Equation 4) [37]:

$$NiSO_{4(s)} + MoO_{3(s)} \rightleftharpoons NiMoO_{4(s)} + SO_{3(g)} \quad (3)$$

$$Na_2SO_{4(s)} + MoO_{3(s)} \rightleftharpoons Na_2MoO_{4(s)} + SO_{3(g)} \quad (4)$$

The calculated formation energies are presented in Table 2. The ΔG (formation Gibbs energy) value is more negative for $NiMoO_4$ formation in reaction 3 as compared to Na_2MoO_4

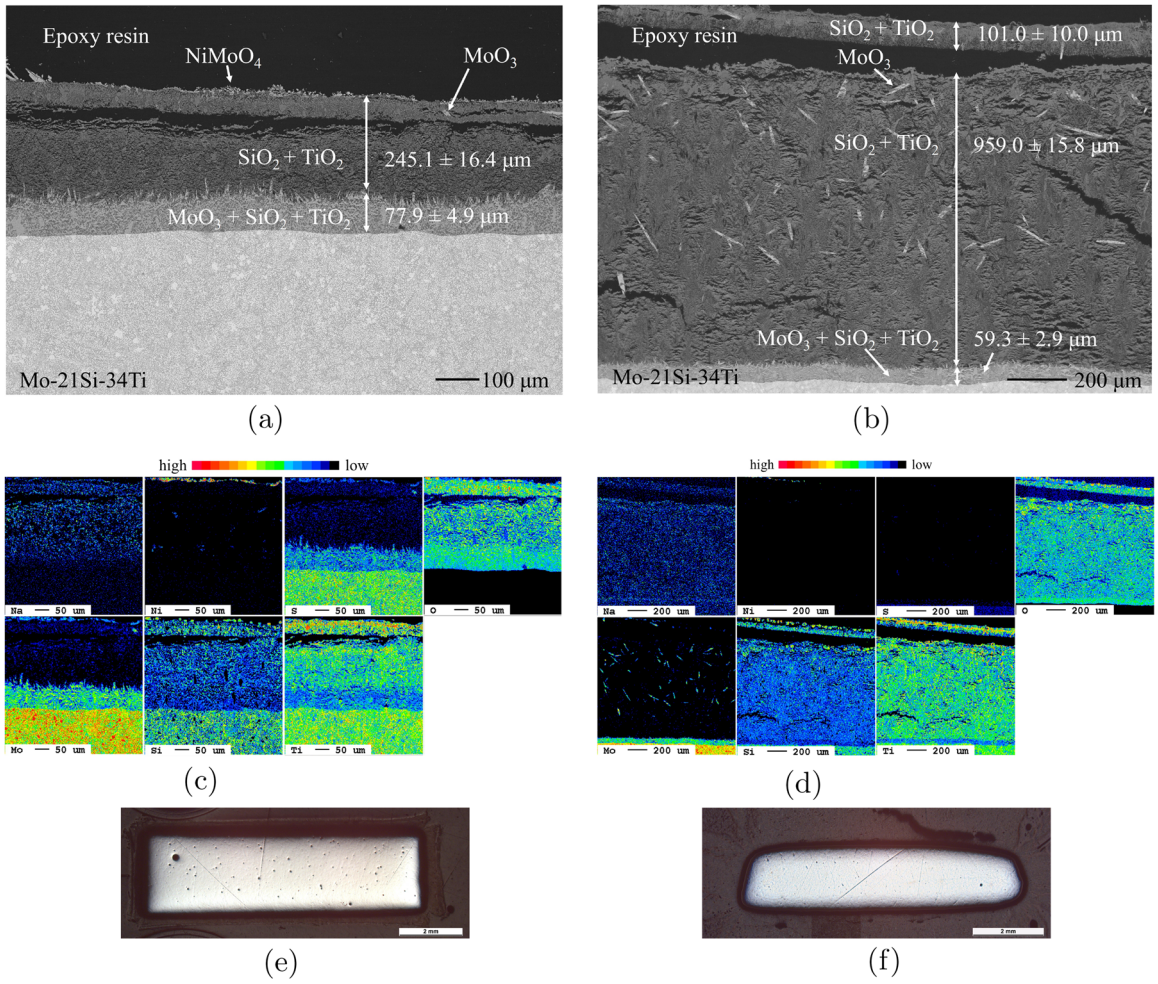

FIGURE 2 | BSE (a,c), EPMA (b,d) and optical microscope images (e,f) of cross-sections after hot corrosion at 700°C in dry synthetic air + 0.1vol.% SO_2 with a $NiSO_4/Na_2SO_4$ deposit. Please note the varying magnification in the respective BSE images. (a) Mo-21Si-34Ti (at.%) after 24 h, (b) Mo-21Si-34Ti (at.%) after 100 h, (c) Mo-21Si-34Ti (at.%) after 24 h, (d) Mo-21Si-34Ti (at.%) after 100 h, (e) Mo-21Si-34Ti (at.%) after 24 h, (f) Mo-21Si-34Ti (at.%) after 100 h. [Color figure can be viewed at wileyonlinelibrary.com]

formation in reaction 4 which indicates that reaction 3 is energetically more favorable under the given conditions. The rapid formation of MoO_3, is reported to occur at temperatures below 700°C [23, 38–40], and thus $NiMoO_4$ forms, which suppresses the presence of the liquid eutectic mixture of Na_2SO_4–$NiSO_4$ responsible for Type II hot corrosion in Ni-based alloys. The thermodynamically more stable $NiMoO_4$ shows a phase transformation of α-$NiMoO_4$ into its high temperature form β-$NiMoO_4$ in the temperature range of 650°C to 720°C, and therefore a mixture of both phases can be assumed to be present at 700°C [41]. In post-testing analysis only α-$NiMoO_4$ could be found, because β-$NiMoO_4$ transforms back to α when cooling below 180°C [42]. Decomposition of $NiMoO_4$ was reported to occur at 730°C and 800°C [42, 43], which rules it out as a potential protective oxide for Mo alloys in future high temperature applications. In the tests conducted at 700°C it is stable and slowed down the corrosion as compared to pure Na_2SO_4, in [28, 29].

Na_2MoO_4 has a relatively low melting point of 678°C [13], resulting in a liquid phase. The eutectic mixture of Na_2MoO_4 and MoO_3 has an even lower melting point of 507°C [44–46]. The liquid phases can dissolve the surrounding material and increase the corrosion rate, as shown for pure Na_2SO_4 deposits in [28].

In the exposure, on the surface of Mo-9Si-8B (at.%) a SiO_2 layer forms and spreads (see Figure 4a), which cannot be dissolved by Na_2MoO_4 [47]. The outer scale must have a low enough viscosity at 700°C which allowed the observed cavities to form. MoO_3 evaporation can be another reason for cavity formation. At higher temperatures [22, 48] low boron additions have a beneficial effect in lowering the melting point and the viscosity of SiO_2, which was not observed here. Otherwise, there would be no pesting during oxidation at 700°C. The presence of $NiMoO_4$ could not affect the SiO_2 layer formation, because neither Ni nor NiO can act as a glass network former or modifier [49]. Incorporation of Na-ions in SiO_2 transforms bridging oxygen to non-bridging oxygen, typically lowering the viscosity [14, 50, 51]. No SiO_2 layer can be seen on the Mo-Si-Ti alloys because it is disrupted by TiO_2. Thus it cannot be definitively determined if the observed changes in the SiO_2 layer are introduced by Na-ions or a combination of Na-ions and B incorporation. The 50 μm thick SiO_2 layer, even though the

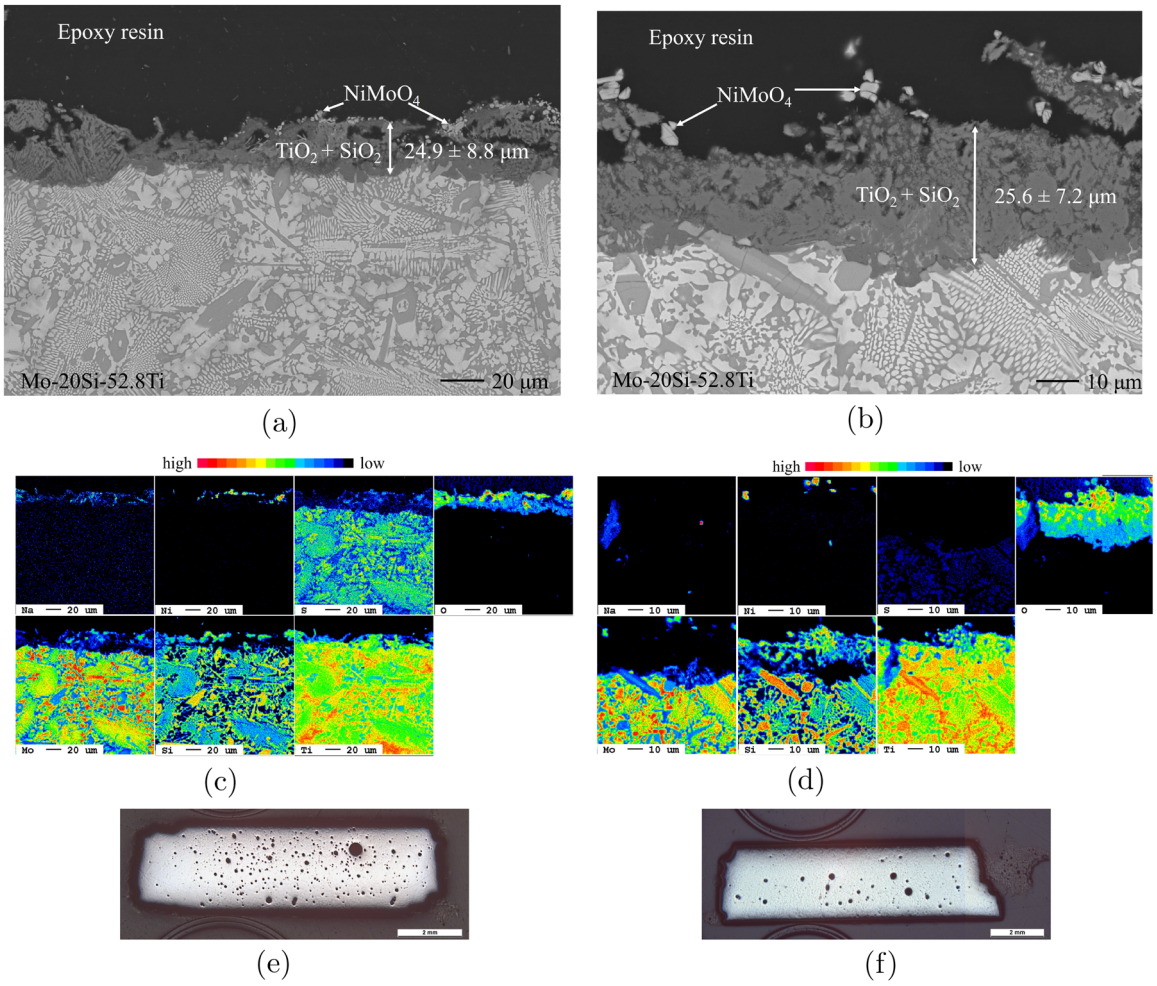

FIGURE 3 | BSE (a,c), EPMA (b,d) and light microscopy (e,f) images of cross-sections after hot corrosion at 700°C in dry synthetic air + 0.1vol.% SO_2 with a $NiSO_4/Na_2SO_4$ deposit. Please note the varying magnifications in the BSE images. (a) Mo-20Si-52.8Ti (at.%) after 24 h, (b) Mo-20Si-52.8Ti (at.%) after 100 h, (c) Mo20Si-52.8Ti after 24 h, (d) Mo-20Si-52.8Ti (at.%) after 100 h, (e) Mo-20Si-52.8Ti (at.%) after 24 h, (f) Mo-21Si-34Ti (at.%) after 100 h. [Color figure can be viewed at wileyonlinelibrary.com]

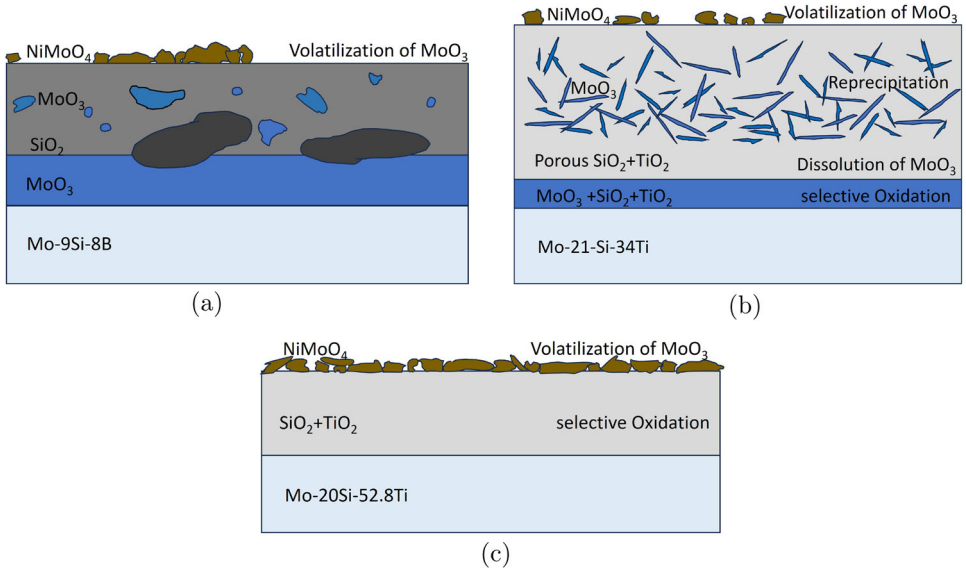

FIGURE 4 | Schematic drawings of the hot corrosion mechanisms of (a) Mo-9Si-8B (at.%), (b) Mo-21Si-34Ti (at.%) and (c) Mo-20Si-52.8Ti (at.%) with a $NiSO_4/Na_2SO_4$ deposit at 700°C in a SO_2-containing atmosphere. [Color figure can be viewed at wileyonlinelibrary.com]

TABLE 2 | Thermodynamic properties of reactions 3 and 4.

Reaction	$\Delta G\,[kJ/mol]$	$\Delta H\,[kJ/mol]$
3: $NiMoO_4 + SO_3$	−188.2	−188.2
4: $Na_2MoO_4 + SO_3$	−98.9	−71.4

material contains only 9% Si, indicates a high amount of alloy was consumed during the experiment, which is confirmed by the 310 μm reduction in cross-section after exposure. The Mo-rich oxide found under the outer scale shows that diffusion and SiO_2 depletion is fast.

The overall oxide scale is much thicker for the Mo-9Si-8B (at.%) sample tested with a pure Na_2SO_4 deposit, which also exhibits more cavities than the sample coated with the Ni-rich mixture of salts [29]. Since the deposit with the mixed salts has a significantly lower Na content, less Na_2MoO_4 can be formed. This can be the reason behind the higher oxygen partial pressure at the corrosion front and therefore higher extent of evaporating MoO_3, despite additional protection from the solid $NiMoO_4$ layer. Local spallation occurred for the samples after 100 h at 700°C, which probably happened during cooling, otherwise the MoO_3 on the surface (see Figure 1b) should have evaporated. Thus the protection from the $NiMoO_4$ layer is likely only temporary, as any thermocycling would reduce the hot corrosion resistance significantly.

After hot corrosion testing at 700°C, the Mo-Si-Ti alloys had a top oxide layer of mixed TiO_2 and SiO_2 (see Figure 4c,b). The eutectic alloy Mo-20Si-52.8Ti (at.%) (see Figure 2) shows significantly higher corrosion resistance compared to the eutectoid alloy Mo-21Si-34Ti (at.%) and Mo-9Si-8B (at.%). The oxide scale reveals a higher TiO_2 content for the Ti-rich alloy than for the eutectoid alloy Mo-21Si-34Ti (at.%) with lower Ti content. Inside the Mo-21Si-34Ti (at.%) outer oxide layer MoO_3 needles were observed in accordance with the fluxing mechanism described in detail in [28]. The oxide layer on Mo-20Si-52.8Ti (at.%) is one order of magnitude thinner (see Figure 3), which can be attributed to the lower Mo content. MoO_3 reacts to form $NiMoO_4$ via Equation 3 which then does not contribute to the further corrosion of the alloy. Due to the lower Mo content in Mo-20Si-52.8Ti (at.%), no Na_2MoO_4 formation was observed. Without Na_2MoO_4 the oxides are not dissolved and the resulting scale is less porous than in the case of the eutectoid alloy. The scale lowers the oxygen partial pressure at the corrosion front and consequently decreases the corrosion rate. This can explain why the increase in thickness of the oxide layer is marginal when comparing the material after 24 and 100 h.

The smaller amount of formed Na_2MoO_4 in the tests with mixed salt deposits lowered the corrosion rate significantly for the Mo-Si-Ti alloys compared to the previous study [28] with pure Na_2SO_4 deposits, while the observed mechanisms stayed the same. For alloys with a higher amount of Mo in their structure $NiSO_4$ is consumed faster. Therefore Na_2MoO_4 can form earlier increasing the corrosion rate. This Mo-content effect leads to a stronger influence of the Ni-containing deposit on alloys with lower Mo-content.

5 | Summary and Conclusion

The hot corrosion resistance of three Mo-based alloys were investigated at 700°C with a deposit of Na_2SO_4 and $NiSO_4$. The resulting attack was compared to that of hot corrosion triggered by pure Na_2SO_4. The hot corrosion behavior varied significantly for the investigated alloys due to their composition, especially the Mo content. The results can be summarized as follows:

- The expected liquid eutectic mixture of Na_2SO_4–$NiSO_4$ could not be detected on any of the samples. It was suppressed by the early formation of $NiMoO_4$.
- The Mo-9Si-8B (at.%) showed formation of SiO_2 with a MoO_3 layer underneath as already observed for the exposure with pure Na_2SO_4. The sample covered with mixed salts revealed a lower corrosion rate because of less Na_2MoO_4 formation from the lower Na content.
- After 24 h of hot corrosion, Mo-21Si-34Ti (at.%) developed a thicker oxide scale compared to Mo-20Si-52.8Ti (at.%). Fluxing of MoO_3 occurred after 100 h and the scale grew rapidly. The sample with pure Na_2SO_4 deposit revealed a higher corrosion rate.
- The Mo-20Si-52.8Ti (at.%) alloy revealed the lowest corrosion rate among the three alloys. It formed a duplex scale consisting of TiO_2 and SiO_2 which was much thicker when only Na_2SO_4 was used as deposit. The attack was progressing slowly for both the eutectic salt mixture of Na_2SO_4/$NiSO_4$ and pure Na_2SO_4.

It can be concluded, that the main driving force for the hot corrosion of the materials is the formation of Na_2MoO_4 which dissolves the surrounding material and therefore prevents the formation of a protective layer. The addition of $NiSO_4$ to the deposit seems to decrease the corrosion rate, as thermodynamic calculations using the FactSage (8.2) Reaction Module indicate that $NiMoO_4$ is more thermodynamically stable than Na_2MoO_4. Consequently, $NiMoO_4$ forms preferentially which delays the formation of Na_2MoO_4 and prevents the Na_2SO_4–$NiSO_4$ eutectic melt. For alloys with a higher Mo content, the molybdates form faster than for low Mo containing alloys. The Mo-content effect explains the difference in the hot corrosion behavior of the two investigated Mo-Si-Ti alloys. In addition $NiMoO_4$ was retained on top as an extra protective layer for the Mo-20Si-52.8Ti (at.%) alloy.

At 700°C the addition of Ni lowers the corrosion rate of the alloys by binding Mo in inactive $NiMoO_4$. Even though $NiMoO_4$ is not stable at higher temperatures, the findings indicate that incorporating supplementary elements capable of binding Mo in stable compounds in a suitable coating may mitigate the corrosion rate of Mo-based alloys. Mg or Ca for example can suppress Na_2MoO_4 via formation of $CaMoO_4$/$MgMoO_4$ which are stable at elevated temperatures [52–54].

The results show that the main corrosion product of Ni based alloys does not increase corrosion rate of Mo-based alloys. Therefore it can be concluded that the usage of Mo-based alloys together with Ni-based alloys does not cause problems

with respect to the hot corrosion behavior of Mo-based alloys.

Author Contributions

Lukas Korell: investigation, writing – original draft preparation, visualization. **Katharina Beck:** methodology, investigation, writing – review and editing, visualization. **Arun Ramasamy Chitra:** thermodynamic calculations, writing. **Frauke Hinrichs:** resources, writing – review and editing. **Ceyhun Oskay:** writing – review and editing, supervision. **Emma White:** writing – review and editing. **Martin Heilmaier:** writing – review and editing, project administration, funding acquisition. **Mathias C. Galetz:** conceptualization, writing – review and editing, supervision, project administration, funding acquisition.

Acknowledgements

The authors thank Dr. Gerald Schmidt for EPMA measurements and Mathias Röhrig for technical support. Many thanks are additionally given to the collaboration partners Daniel Schliephake and Martin Heilmaier from the Institute for Applied Materials (IAM-WK), Karlsruhe Institute of Technology (KIT), for providing the Mo-9Si-8B alloy. This work was supported by the Research Training Group 2561 "MatCom-ComMat: Materials Compounds from Composite Materials for Applications in Extreme Conditions" (project number: 413956820) funded by the Deutsche Forschungsgemeinschaft (DFG).

Conflicts of Interest

The authors declare no conflicts of interest.

Data Availability Statement

The data that support the findings of this study are available from the corresponding author upon reasonable request.

References

1. L. Jiang, B. Zheng, C. Wu, et al., "A Review of Mo-Si Intermetallic Compounds as Ultrahigh-Temperature," *Processes* 10, no. 9 (2022): 1772, https://doi.org/10.3390/pr10091772.

2. J. H. Perepezko, "The Hotter the Engine, the Better," *Science* 326, no. 5956 (2009): 1068–1069, https://doi.org/10.1126/science.1179117.

3. B. Rapp, "Coatings Improve Efficiency," *Materials Today* 9, no. 7–8 (2006): 6, https://doi.org/10.1016/S1369-7021(06)71555-3.

4. D. M. Dimiduk and J. H. Perepezko, "MoSi-B Alloys: Developing a Revolutionary Turbine-Engine Material," *MRS Bulletin* 28, no. 09 (2003): 639–645, https://doi.org/10.1557/mrs2003.191.

5. D. Schliephake, A. Kauffmann, X. Cong, et al., "Constitution, Oxidation and Creep of Eutectic and Eutectoid Mo-Si-Ti Alloys," *Intermetallics* 104 (2019): 133–142, https://doi.org/10.1016/j.intermet.2018.10.028.

6. L. Yu, Y. Zhang, T. Fu, J. Wang, K. Cui, and F. Shen, "Rare Earth Elements Enhanced the Oxidation Resistance of Mo-Si-Based Alloys for High Temperature Application: A Review," *Coatings* 11, no. 9 (2021): 1144, https://doi.org/10.3390/coatings11091144.

7. N. Eliaz, G. Shemesh, and R. M. Latanision, "Hot Corrosion in Gas Turbine Components," *Engineering Failure Analysis* 9, no. 1 (2002): 31–43, https://doi.org/10.1016/S1350-6307(00)00035-2.

8. D. A. Shifler, "Hot Corrosion: A Modification of Reactants Causing Degradation," *Materials at High Temperatures* 35, no. 1–3 (2018): 225–235, https://doi.org/10.1080/09603409.2017.1404692.

9. G. H. Meier, "Invited Review Paper In Commemoration of over 50 Years of Oxidation of Metals: Current Aspects of Deposit-Induced Corrosion," *Oxidation of Metals* 98, no. 1–2 (2022): 1–41, https://doi.org/10.1007/s11085-020-10015-6.

10. W. T. Reid, *External Corrosion and Deposits: Boilers and Gas Turbines* (American Elsevier Publishing Co., Inc., 1971).

11. B. Grégoire, X. Montero, M. C. Galetz, G. Bonnet, and F. Pedraza, "Mechanisms of Hot Corrosion of Pure Nickel at 700°C: Influence of Testing Conditions," *Corrosion Science* 141 (2018): 211–220, https://doi.org/10.1016/j.corsci.2018.06.009.

12. F. Pettit, "Hot Corrosion of Metals and Alloys," *Oxidation of Metals* 76, no. 1–2 (2011): 1–21, https://doi.org/10.1007/s11085-011-9254-6.

13. B. S. Lutz, J. M. Alvarado-Orozco, L. Garcia-Fresnillo, and G. H. Meier, "Na_2SO_4-Deposit-Induced Corrosion of Mo-Containing Alloys," *Oxidation of Metals* 88, no. 5–6 (2017): 599–620, https://doi.org/10.1007/s11085-017-9746-0.

14. M. Taylor and J. H. Perepezko, "Hot Corrosion of Mo-Si-B Coatings," *Oxidation of Metals* 87, no. 5–6 (2017): 705–715, https://doi.org/10.1007/s11085-017-9773-x.

15. P. Kofstad and G. Akesson, "Sulfate-Induced High-Temperature Corrosion of Nickel," *Oxidation of Metals* 14 (1980): 301–323, https://doi.org/10.1007/BF00603787.

16. R. A. Rapp, "Hot Corrosion of Materials: A Fluxing Mechanism?," *Corrosion Science* 44 (2002): 209–221, https://doi.org/10.1016/S0010-938X(01)00057-9.

17. H. H. Strehblow, V. Maurice, and P. Marcus, Passivity of Metals. *3* (CRC Press, Taylor and Francis, 2011).

18. N. S. Bornstein, "Reviewing Sulfidation Corrosion—Yesterday and Today," *JOM* 48, no. 11 (1996): 37–39, https://doi.org/10.1007/BF03223242.

19. J. Stringer, "High-Temperature Corrosion of Superalloys," *Materials Science and Technology* 3, no. 7 (1987): 482–493, https://doi.org/10.1080/02670836.1987.11782259.

20. J. Sumner, A. Encinas-Oropesa, N. J. Simms, and J. R. Nicholls, "Type II Hot Corrosion: Kinetics Studies of CMSX-4," *Oxidation of Metals* 80 (2013): 553–563, https://doi.org/10.1007/s11085-013-9395-x.

21. S. Obert, A. Kauffmann, and M. Heilmaier, "Characterisation of the Oxidation and Creep Behaviour of Novel Mo-Si-Ti Alloys," *Acta Materialia* 184 (2020): 132–142, https://doi.org/10.1016/j.actamat.2019.11.045.

22. T. A. Parthasarathy, M. G. Mendiratta, and D. M. Dimiduk, "Oxidation Mechanisms in Mo-Reinforced Mo_5SiB_2(T2)–Mo3Si Alloys," *Acta Materialia* 50 (2002): 1857–1868, https://doi.org/10.1016/S1359-6454(02)00039-3.

23. K. Pan, Y. Yang, S. Wei, et al., "Oxidation Behavior of Mo-Si-B Alloys at Medium-To-High Temperatures," *Journal of Materials Science & Technology* 60 (2021): 113–127, https://doi.org/10.1016/j.jmst.2020.06.004.

24. S. Obert, A. Kauffmann, R. Pretzler, D. Schliephake, F. Hinrichs, and M. Heilmaier, "The Creep and Oxidation Behaviour of Pesting-Resistant $(Mo,Ti)_5Si_3$-Containing Eutectic-Eutectoid Mo-Si-Ti Alloys," *Metals* 11, no. 1 (2021): 169, https://doi.org/10.3390/met11010169.

25. S. Obert, A. Kauffmann, S. Seils, et al., "Microstructural and Chemical Constitution of the Oxide Scale Formed on a Pesting-resistant Mo-Si-Ti Alloy," *Corrosion Science* 178 (2021): 109081, https://doi.org/10.1016/j.corsci.2020.109081.

26. F. Hinrichs, A. Kauffmann, A. S. Tirunilai, et al., "A Novel Nitridation-And Pesting-Resistant Cr-Si-Mo Alloy," *Corrosion Science* 207 (2022): 110566, https://doi.org/10.1016/j.corsci.2022.110566.

27. G. C. Fryburg, F. J. Kohl, C. A. Stearns, and W. L. Fielder, "Chemical Reactions Involved in the Initiation of Hot Corrosion of B-1900 and NASA-TRW Via," *Journal of the Electrochemical Society* 129, no. 3 (1982): 571–585, https://doi.org/10.1002/chin.198227029.

28. K. Beck, T. König, E. Senvardarli, F. Hinrichs, M. Heilmaier, and M. C. Galetz, "Hot Corrosion Behavior of Mo–Si–Ti Alloys," *Materials and Corrosion* 75, no. 12 (2024): 1610–1619, https://doi.org/10.1002/maco.202414491.

29. K. Beck, T. König, A. Case, C. Oskay, and M. C. Galetz, "Hot Corrosion Behavior of Mo–9.0Si–8.0B," *Materials and Corrosion* 75, no. 12 (2024): 1600–1609, https://doi.org/10.1002/maco.202414347.

30. N. Birks, G. H. Meier, and F. S. Pettit, *Introduction to the High Temperature Oxidation of Metals* (Cambridge University Press, 2012).

31. D. Yu Fluidized bed Selective Oxidation and Sulfation Roasting of Nickel Sulfide Concentrate (PhD thesis. University of Toronto, 2013).

32. G. Li, H. Cheng, S. Chen, X. Lu, Q. Xu, and C. Lu, "Mechanism of Na_2SO_4 Promoting Nickel Extraction From Sulfide Concentrates by Sulfation Roasting–Water Leaching," *Metallurgical and Materials Transactions B* 49, no. 3 (2018): 1136–1148, https://doi.org/10.1007/s11663-018-1214-y.

33. M. Zahiri Azar, T. Gheno, B. Gleeson, and A. H. Heuer, "Initial Stages of Na_2SO_4-Induced Degradation of β-Ni–36Al at 700°C: I-Intrinsic Behavior," *Oxidation of Metals* 88, no. 5–6 (2017): 649–667, https://doi.org/10.1007/s11085-017-9760-2.

34. C. Hochmuth, D. Schliephake, R. Völkl, M. Heilmaier, and U. Glatzel, "Influence of Zirconium Content on Microstructure and Creep Properties of Mo-9Si–8B Alloys," *Intermetallics* 48 (2014): 3–9, https://doi.org/10.1016/j.intermet.2013.08.017.

35. S. Burk, B. Gorr, V. B. Trindade, U. Krupp, and H. J. Christ, "High Temperature Oxidation of Mechanically Alloyed Mo–Si–B Alloys," *Corrosion Engineering, Science and Technology* 44, no. 3 (2009): 168–175, https://doi.org/10.1179/174327809X419122.

36. M. Zhao, W. Ye, M. Zhu, et al., "From Mo-Si-B to MoTi-Si-B Alloys: A Short Review," *Materials (Basel, Switzerland)* 16, no. 1 (2022): 3, https://doi.org/10.3390/ma16010003.

37. A. K. Misra, "Mechanism of Na_2SO_4 – Induced Corrosion of Molybdenum Containing Nickel–Base Superalloys at High Temperatures: I. Corrosion in Atmospheres Containing Only," *Journal of the Electrochemical Society* 133, no. 5 (1986): 1029–1038, https://doi.org/10.1149/1.2108700.

38. M. Simnad and A. Spilners, "Kinetics and Mechanism of the Oxidation of Molybdenum," *JOM* 7 (1955): 1011–1016, https://doi.org/10.1007/BF03377603.

39. E. A. Gulbransen, K. F. Andrew, and F. A. Brassart, "Oxidation of Molybdenum 550 to 1700°C," *Journal of the Electrochemical Society* 110, no. 9 (1963): 952, https://doi.org/10.1149/1.2425918.

40. P. J. Meschter, "Low-Temperature Oxidation of Molybdenum Disilicide," *Metallurgical Transactions A* 23 (1992): 1763–1772, https://doi.org/10.1007/BF02804369.

41. A. Kaddouri, E. Tempesti, and C. Mazzocchia, "Comparative Study of β-Nickel Molybdate Phase Obtained by Conventional Precipitation and the Sol-Gel Method," *Materials Research Bulletin* 39, no. 4–5 (2004): 695–706, https://doi.org/10.1016/j.materresbull.2003.11.005.

42. B. Moreno, E. Chinarro, M. T. Colomer, and J. R. Jurado, "Combustion Synthesis and Electrical Behavior of Nanometric β-$NiMoO_4$," *Journal of Physical Chemistry C* 114, no. 10 (2010): 4251–4257, https://doi.org/10.1021/jp907870a.

43. J. A. Rodriguez, S. Chaturvedi, J. C. Hanson, A. Albornoz, and J. L. Brito, "Electronic Properties and Phase Transformations in $CoMoO_4$ and $NiMoO_4$: XANES and Time-Resolved Synchrotron XRD Studies," *Journal of Physical Chemistry B* 102, no. 8 (1998): 1347–1355, https://doi.org/10.1021/jp972137q.

44. R. Amin Solid State Electrochemical Characterization of Thermodynamic Properties of Sodium-Metal-Oxygen Systems (PhD thesis. Universität Stuttgart, 2005).

45. A. Navrotsky and O. J. Kleppa, "Calorimetric Study of Molten Sodium Molybdate-Molybdenum Trioxide Mixtures at 970.Degree.K," *Inorganic Chemistry* 6 (1967): 2119–2121, https://doi.org/10.1021/ic50057a047.

46. F. Hoermann, "Beitrag zur Kenntnis der Molybdate und Wolframate. Die Binären Systeme:Li_3MoO_4-MoO_3, Na_2MoO_4-MoO_3, K_3MoO_4-MoO_3, Li_2WO_4-WO_3, $Na_2WO_4WO_3$, K_2WO_4-WO_3, Li_2MoO_4-Na_2MoO_4, $Li_2WO_4Na_2WO_4$, Li_2MoO_4-K_2MoO_4," *Zeitschrift für Anorganische und Allgemeine Chemie* 177, no. 1 (1929): 145–186, https://doi.org/10.1002/zaac.19291770117.

47. D. Gorman-Lewis, L. Mazeina, J. B. Fein, J. E. S. Szymanowski, P. C. Burns, and A. Navrotsky, "Thermodynamic Properties of Soddyite From Solubility and Calorimetry Measurements," *Journal of Chemical Thermodynamics* 39 (2007): 568–575, https://doi.org/10.1016/j.jct.2006.09.005.

48. C. Gatzen, I. Smokovich, M. Scheffler, and M. Krüger, "Oxidation Resistant Environmental Barrier Coatings for Mo–Based Alloys: A Review," *Advanced Engineering Materials* 23, no. 4 (2020): 23, https://doi.org/10.1002/adem.202001016.

49. J. Jiusti, E. D. Zanotto, S. A. Feller, et al., "Effect of Network Formers and Modifiers on the Crystallization Resistance of Oxide Glasses," *Journal of Non-Crystalline Solids* 550 (2020): 120359, https://doi.org/10.1016/j.jnoncrysol.2020.120359.

50. A. Abd El-Moneim, "Quantitative Analysis of Elastic Moduli and Structure of B_2O_3–SiO_2 and Na_2O–B_2O_3–SiO_2 Glasses," *Physica B: Condensed Matter* 325 (2003): 319–332, https://doi.org/10.1016/S0921-4526(02)01545-4.

51. H. Jabraoui, Y. Vaills, A. Hasnaoui, M. Badawi, and S. Ouaskit, "Effect of Sodium Oxide Modifier on Structural and Elastic Properties of Silicate Glass," *Journal of Physical Chemistry B* 120, no. 51 (2016): 13193–13205, https://doi.org/10.1021/acs.jpcb.6b09664.

52. A. Chychko, L. Teng, and S. Seetharaman, "MoO3Evaporation Studies From Binary Systems Towards Choice of Mo Precursors in EAF," *Steel Research International* 81, no. 9 (2010): 784–791, https://doi.org/10.1002/srin.201000055.

53. V. Massarotti, G. Flor, A. Marini, and R. Riccardi, "Molybdates Solid State Synthesis: The MgO—MoO_3 System," *Zeitschrift für Naturforschung A* 35, no. 5 (1980): 500–502, https://doi.org/10.1515/zna-1980-0506.

54. E. K. Kazenas, Y. V. Tsvetkov, G. K. Astakhova, and V. A. Volchenkova, "Thermodynamics of the Sublimation of Calcium Molybdate," *Russian Metallurgy (Metally)* 2006 (2006): 147–149, https://doi.org/10.1134/S003602950602008X.

55. M. Dieterle, G. Weinberg, and G. Mestl, "Raman Spectroscopy of Molybdenum Oxides," *Physical Chemistry Chemical Physics* 4, no. 5 (2002): 812–821, https://doi.org/10.1039/B107012F.

Appendix

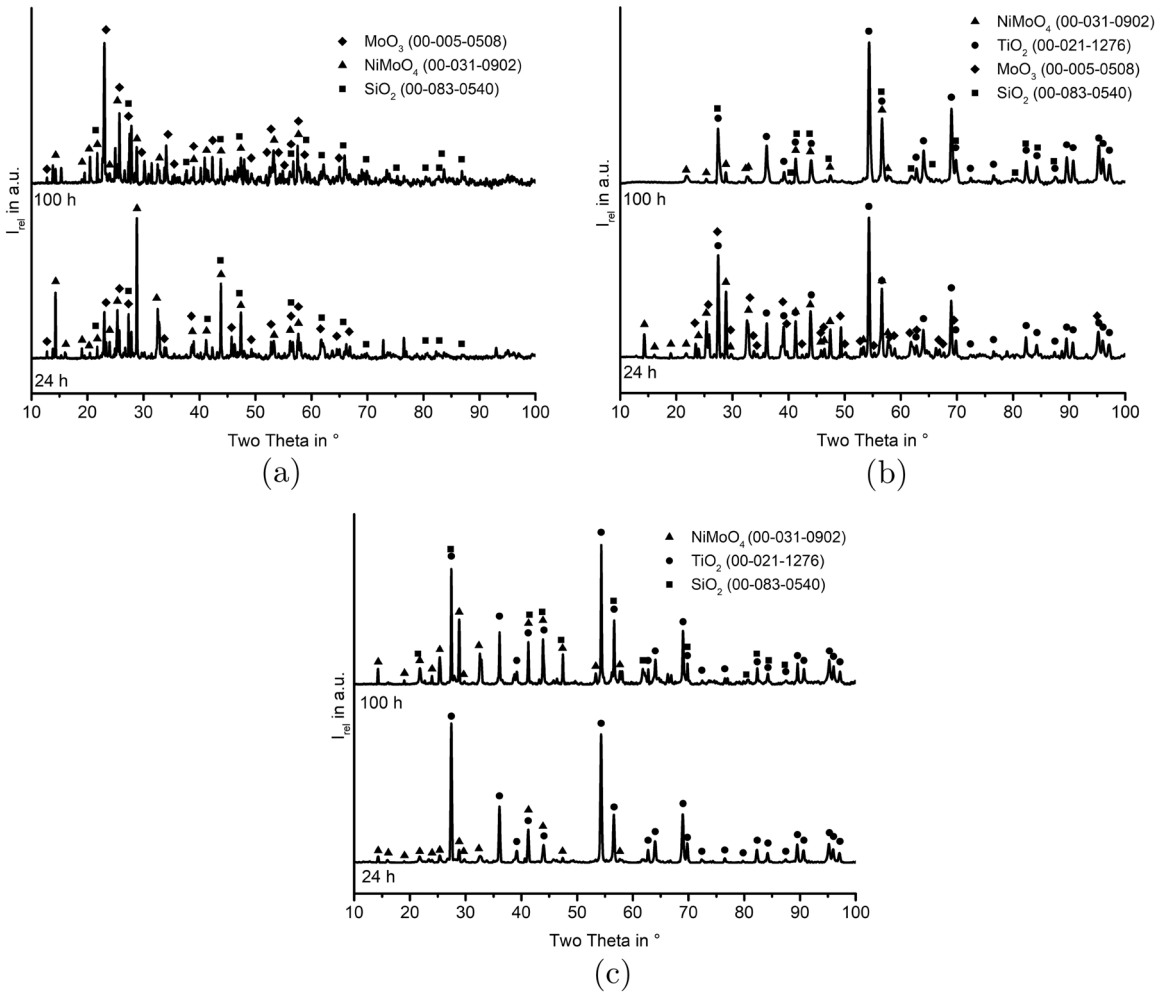

FIGURE A1 | XRD patterns of (a) Mo-9Si-8B (at.%), (b) Mo-21Si-34Ti (at.%) and (c) Mo-20Si-52.8Ti (at.%) after 24 and 100 h of hot corrosion.

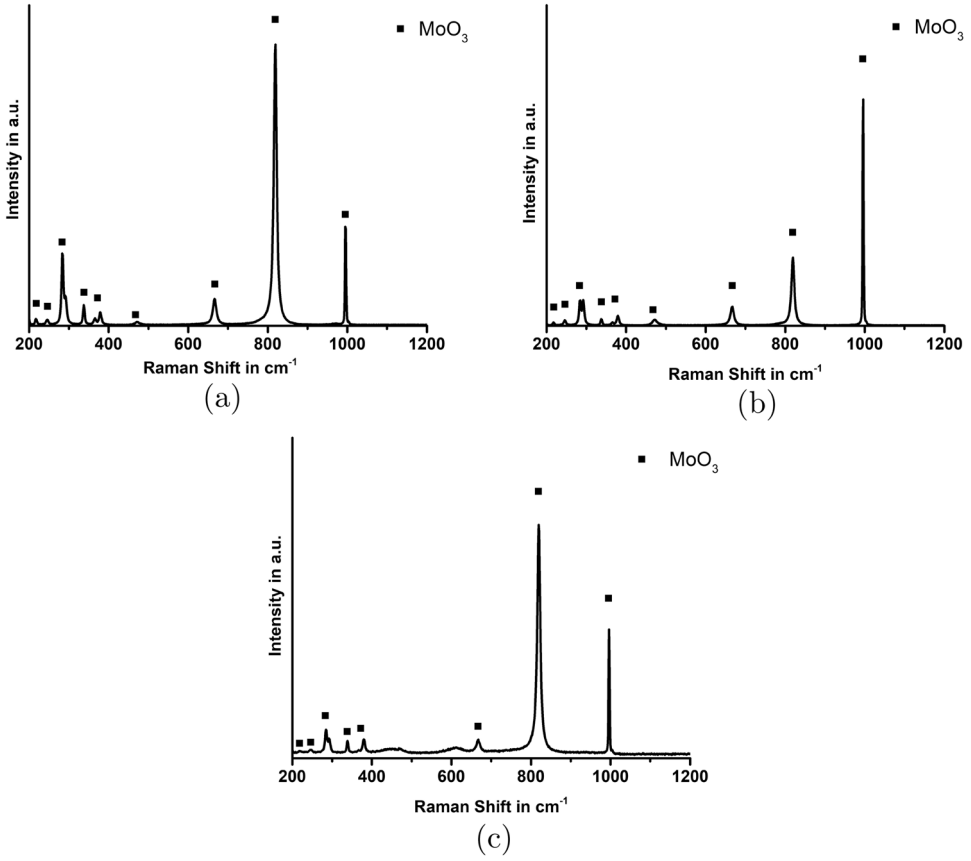

FIGURE A2 | Raman spectra of the Mo oxides formed on (a) Mo-9Si-8B (at.%) after 24 h, (b) Mo-9Si-8B (at.%) after 100 h and (c) Mo-20Si-52.8Ti (at.%) after 100 h of hot corrosion compared to MoO_3 Raman spectra from [55].